

Article

Zn-Co-Mo-rGO Ultra-Thin Nanosheets Arrays-Based Electrode Materials for Asymmetric Supercapacitor

Shuang Liu¹, Siwei He¹, Yanhong Xiang¹, Xiaochun Peng², Lizhi Xiong³ and Jianhua Wu^{1,*}¹ College of Physics and Electromechanical Engineering, Jishou University, Jishou 416000, China² College of Chemistry and Chemical Engineering, Jishou University, Jishou 416000, China³ College of Pharmacy, Jishou University, Jishou 416000, China

* Correspondence: jianhuawu@jsu.edu.cn

Abstract: The design of electrode materials for supercapacitors (SCs) with high specific capacity and high energy density has always been a research hotspot. In this paper, ternary metal oxides Zn-Co-Mo-rGO (ZCMG) and Zn-Co-Mo (ZCM) based electrode materials were prepared by one-step hydrothermal method. Compared with the ZCM, SEM and TEM results demonstrates the ultra-thin nanosheets grown vertically on the nickel foam for ZCMG. Owing to synergistic effect of the multi-component composites, the as-prepared electrode with ZCMG exhibits the specific capacity of 713 C g⁻¹ (1189 F g⁻¹) at 1 A g⁻¹, which was higher than that of ZCM without rGO (492 F g⁻¹, 295 C g⁻¹). The assembled ZCMG//AC (activated carbon) asymmetric supercapacitor (ASC) delivers the maximum specific capacity of 68 C g⁻¹ (45 F g⁻¹) at 1 A g⁻¹. After 1000 cycles, it still has a high-capacity retention rate of 95%. Furthermore, the ASC exhibited an energy density of 14 Wh kg⁻¹ at 750 W kg⁻¹, and it can retain 5.23 Wh kg⁻¹, even at 7500 W kg⁻¹.

Keywords: supercapacitor; ternary metal oxide; reduced graphene oxide; ultra-thin nanosheet



Citation: Liu, S.; He, S.; Xiang, Y.; Peng, X.; Xiong, L.; Wu, J. Zn-Co-Mo-rGO Ultra-Thin Nanosheets Arrays-Based Electrode Materials for Asymmetric Supercapacitor. *Batteries* **2023**, *9*, 158. <https://doi.org/10.3390/batteries9030158>

Academic Editor: Atsushi Nagai

Received: 2 February 2023

Revised: 27 February 2023

Accepted: 28 February 2023

Published: 2 March 2023



Copyright: © 2023 by the authors. Licensee MDPI, Basel, Switzerland. This article is an open access article distributed under the terms and conditions of the Creative Commons Attribution (CC BY) license (<https://creativecommons.org/licenses/by/4.0/>).

1. Introduction

Due to the energy crisis and environmental pollution issued from extensive fossil fuels consumption, clean energy, such as solar, wind, and tidal energy, occupies an increasingly important position. Such energy supplies are intermittent, hence energy storage devices with high energy density, power density, and long cycle stability are required. Among them, supercapacitors (SCs) possess high power density [1], long cycle life, and high charge-discharge rates [2]. However, the relatively low energy density hindered their large-scale commercialization. According to the formula of energy density $E = 1/2 CV^2$ [3], the energy density can be improved by increasing the voltage window (V) of SCs and the specific capacity (C) of electrode materials [4,5].

The electrode material is one of the most important factors affecting the performance of supercapacitors. Transition metal oxides (TMOs) are typical pseudocapacitive electrode materials, and single-metal oxide electrode materials with low prices and high abundance, such as MnO₂, Fe₃O₄, NiO, ZnO, and Co₃O₄, have been widely studied. However, their poor conductivity is adverse to electron transport [6]. For instance, NiO with nanospheres and nanobelts structures only delivered the specific capacitances of 45.2 and 556.2 F g⁻¹ at a current density of 1 A g⁻¹, respectively [7]. ZnO nanomembranes synthesized by atomic layer deposition displayed the largest capacitance of 846 F g⁻¹ in 6 M KOH electrolyte at 1 A g⁻¹ [8]. Besides, due to the high theoretical energy storage capacity (3560 F g⁻¹), Co₃O₄ could be a candidate for SC electrode materials [9]. While the hexagonal Co₃O₄ electrode presented the specific capacitance of 216.4 F g⁻¹ at 1 A g⁻¹ [10], oxygen-vacancy abundant ultrafine Co₃O₄ nanoparticles/graphene composites electrode delivered the specific capacitance of 978.1 F g⁻¹ at 1 A g⁻¹. All the results are far below the theoretical energy storage capacity due to the poor conductivity and lack of electroactive sites on the surface [9]. Construction of hollow hierarchically micro-/nanostructures could

improve their electrochemical properties because of the high specific surface area. The Co_3O_4 hollow microspheres displayed the specific capacitance of 394.4 F g^{-1} at 2 A g^{-1} , the unique hierarchical multishelled structure enlarged the contact area of the electrode and electrolyte and provided easy electrolyte penetration path. However, its specific capacity should still be improved further [11]. Doping is another strategy to elevate the performance of electrode materials. Mo-doping changed the morphology of NiO nanomaterials and enlarged the active surface area and active sites, resulting the improved specific capacitance of 1096.64 F g^{-1} [12]. Furthermore, appropriate doping could also optimize the electronic structure of the host materials [13]. Compared with single-metal oxides, multi-metallic oxides have more elements involved in redox reactions, and the synergistic effects of multiple elements could generate better electrochemical performance [14–16]. For example, NiCo_2O_4 hollow microspheres presented a specific capacitance of 764 F g^{-1} at 2 A g^{-1} [17]. Recently, trimetallic oxide-based electrode materials have gradually attracted the people's attention, and metal ions with multivalent were selected. Zn-Fe-Co oxide nanowires delivered a maximum specific capacitance of 1297.4 F g^{-1} at 1 A g^{-1} , and the capacity retention rate was 95% even after 5000 cycles [18]. Acharya et al. [19] prepared a flower-like Zn-Ni-Co oxide with a specific capacity of 259 mAh g^{-1} at 1 A g^{-1} . Yuan et al. [20] synthesized one-dimensional mesoporous Co-Ni-Mn oxide nanowires with pseudocapacitance of 612 F g^{-1} at 0.5 A g^{-1} , and the capacity decay is 0.28% per 100 cycles over 5000 cycles at 10 A g^{-1} . Binder-free Zn-Mn-Co ternary oxide nanoneedles presented the specific capacity of 849 C g^{-1} at 1 A g^{-1} and high coulombic efficiency of 99.5% after 10,000 cycles [21]. In consequence, TMOs with multiple components could present better performance than single metal oxides and bimetallic oxides benefit from the synergistic effect of different metal ions [22]. Nevertheless, these materials still have the disadvantages of low conductivity and poor cycle stability. For example, flower-like Zn-Co-Mo ternary metal oxide displayed higher electrochemical performance than that of $\text{ZnCo}_2\text{O}_4/\text{Ni}$ and CoMoO_4/Ni composites and showed a specific capacitance of 384 F g^{-1} , while it only displayed a capacity retention rate of 81.25% after 1000 cycles [23].

The introduction of carbon nanocomposites could be useful strategy to overcome the problems above [24], and reduced graphene oxide (rGO) is widely used in SCs due to its large specific surface area and good conductivity [25]. The synergistic effects of rGO and multi-metallic oxides could accelerate the electron transfer process. For example, the introduction of rGO could provide the mesopore characteristics with a higher pore volume and guarantee the higher transmission of electrolyte ions, as well as the higher surface Faradic redox reactions. For instance, SCs with $\text{ZnFe}_2\text{O}_4/\text{rGO}$ [26], $\text{MnNb}_2\text{O}_6/\text{rGO}$ [27], and $\text{Mn}_{0.1}\text{Ni}_{0.9}\text{MoO}_4/\text{rGO}$ [28] electrode materials displayed superior electrochemical performance compared to electrode materials without rGO.

Herein, to improve the specific capacitance and cycle performance of Zn-Co-Mo ternary metal oxide, ZCMG and ZCM ternary metal oxides with and without rGO were synthesized via hydrothermal method, and significant improvements in morphology and electrochemical performance were observed as a result of the synergistic effect of rGO and ZCM. The presence of rGO effectively improved the dispersibility, adjusted the thickness and structure of ZCM, as well as the improved conductivity. Self-supporting ZCMG nanosheets were grown on nickel foam (NF) to form a cross-linked network, and this nanostructure facilitates charge transfer and electrolyte diffusion. The specific capacity of ZCMG electrode material is 713 C g^{-1} at 1 A g^{-1} . After being assembled into SCs, the maximum specific capacity is 68 C g^{-1} . After 1000 cycles, it has a high-capacity retention rate (95%). The energy density is 14 Wh kg^{-1} at a power density of 750 W kg^{-1} , and it remains 5.23 Wh kg^{-1} at 7500 W kg^{-1} . Although the research on ZCM has been reported, there are relatively few studies using ZCMG as electrode material for supercapacitors. All the above results show that ZCMG material is expected to become a new generation of electrode material for SCs.

2. Materials and Methods

2.1. Materials

$\text{Zn}(\text{NO}_3)_2 \cdot 6\text{H}_2\text{O}$, $(\text{NH}_4)_6\text{Mo}_7\text{O}_{24} \cdot 4\text{H}_2\text{O}$, $\text{Co}(\text{NO}_3)_2 \cdot 6\text{H}_2\text{O}$, hydrochloric acid, ethanol, urea, and KOH were all purchased from Shanghai Energy Chemical Co., Ltd. All chemicals used were analytical grade and used as received [29,30]. rGO (98%) was purchased from Suzhou Tanfeng Graphene Technology Co., Ltd. (Suzhou, China). Nickel foam (NF) was purchased from Suzhou Keshenghe Metal Materials Co., Ltd. (Suzhou, China).

2.2. Synthesis of Electrode Materials

The NFs were successively ultrasonic washed in 2 M hydrochloric acid, deionized (DI) water, absolute acetone, and ethanol for 15 min, and then they were dried in vacuum at 60 °C for 12 h. As depicted in Figure 1, $\text{Zn}(\text{NO}_3)_2 \cdot 6\text{H}_2\text{O}$ (1 mmol, 0.29 g), $\text{Co}(\text{NO}_3)_2 \cdot 6\text{H}_2\text{O}$ (2 mmol, 0.58 g), $(\text{NH}_4)_6\text{Mo}_7\text{O}_{24} \cdot 4\text{H}_2\text{O}$ (2 mmol, 2.47 g), and urea (5 mmol, 0.3 g) were dissolved in DI water (100 mL) and stirred for 1 h to obtain a pink solution, then 4 mL of rGO dispersion in water (1 mg/mL) was added. After stirring for 1 h, the solution was transferred into a 100 mL Teflon-lined stainless-steel autoclave, and another NF fixed on a Teflon skeleton was placed in the solution and subjected to hydrothermal reaction at 130 °C for 6 h. After cooling to room temperature, the sample was taken out and washed with DI water and ethanol alternately for several times. The sample was dried in vacuum for 8 h and then calcinated at 300 °C for 2 h at a heating rate of 2 °C/min to generate ZCMG. By comparison, during the preparation procedure of ZCM, no rGO dispersion was added. Both the average mass loading of as-fabricated ZCM and ZCMG were 1.1 mg cm⁻² [31].

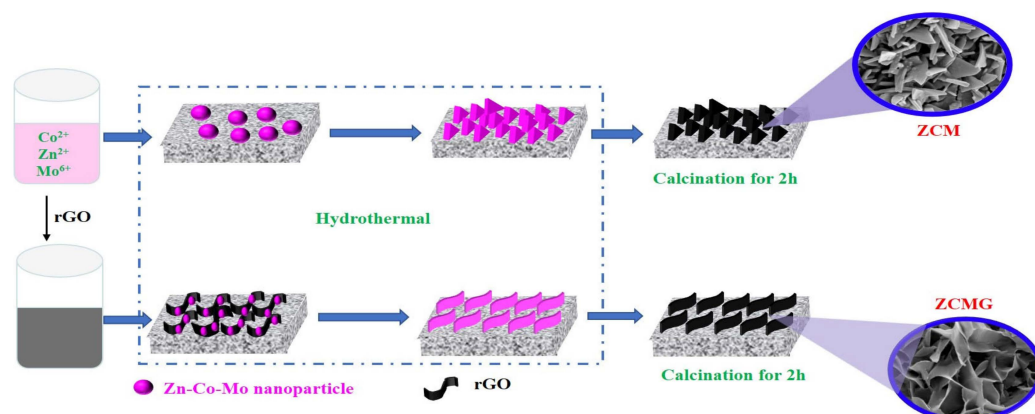


Figure 1. Synthesis route of ZCMG and ZCM nanosheets on NF.

2.3. Structure Characterization

Scanning electron microscope (SEM, Zeiss Sigma 300, Oberkochen, Germany) were employed to characterize the morphology and microstructure of the electrode materials, the transmission electron microscope (TEM, FEI Titan G2 60-300, Brno, Czech Republic) with an energy dispersive spectrometer (EDS), and selected area electron diffraction (SAED) under an acceleration voltage of 200 kV was used for specific features of the materials. X-ray diffractometer (XRD, Panalytical Empyrean, Almelo, The Netherlands) confirmed the crystal structure of the materials at a scanning speed of 2° min⁻¹ with Cu K α radiation ($\lambda = 1.5408 \text{ \AA}$). The chemical surface state and composition of the materials were characterized by X-ray photoelectron spectroscopy (XPS, Thermo Scientific ESCALAB Xi+, Thermo Fisher Scientific Inc., Waltham, MA, USA) with an Al K α exciting source (1486.6 eV) and correct the C 1 s peak at 284.8 eV before sample analysis. The specific surface area and corresponding pore size distribution of the materials were investigated based on nitrogen adsorption–desorption isotherms (Micrometitics ASAP 2020, Norcross, GA, USA) at 77 K via Brunauer-Emmett-Teller (BET) method and Barrett-Joyner-Halenda (BJH) models.

2.4. Electrochemical Measurements

The electrochemical performance was investigated by two-electrode and three-electrode measurements on CHI760E electrochemical workstation. In three-electrode measurements, ZCM or ZCMG was used as the working electrode ($A = 1 \times 1 \text{ cm}^2$), Pt foil ($A = 1 \times 1 \text{ cm}^2$), and saturated calomel electrode (SCE) were used as counter electrode and reference electrode, and 2 M KOH aqueous solution acted as electrolyte. ASCs were also assembled by using ZCMG or ZCM cathode and activated carbon (AC) anode. The anode was prepared by varnishing a homogeneous slurry onto a piece of NF ($1 \text{ cm} \times 1 \text{ cm}$), which was composed of active materials (80% in mass), acetylene clack (10% in mass), and PVDF (10% in mass) mixed in N-methylpyrrolidone, followed by a drying process in vacuum for 8 h. The specific capacity ($C, \text{C g}^{-1}$), energy density ($E, \text{Wh kg}^{-1}$), and power density ($P, \text{W kg}^{-1}$) were calculated via the following equations [32,33]:

$$C = I \times \Delta t / m \quad (1)$$

$$E = 0.5 \times C \times \Delta V / 3.6 \quad (2)$$

$$P = E \times 3600 / \Delta t \quad (3)$$

where I , Δt , m , and ΔV represent the current, discharge time, mass of active material, and voltage window, respectively.

3. Results and Discussion

ZCM and ZCMG pseudocapacitive self-supporting electrodes were successfully constructed on NF by a one-step hydrothermal method combined with calcination process. During the hydrothermal reaction, urea was decomposed into NH_3 at high temperature and OH^- was further produced to provide an alkaline environment. Further, Zn^{2+} , Co^{2+} , and Mo^{6+} could convert to their corresponding hydroxide precursor (ZCM-OH). As depicted in Figure 1, during the formation of ZCM, the nanoparticles are more likely to aggregate and finally form sheets with a certain thickness. For the preparation of ZCMG, rGO was first deposited on the NF, and ZCM nanoparticles were subsequently distributed on the rGO sheets. Due to the large specific surface area and good dispersion of rGO, ZCM was uniformly dispersed to form thinner nanosheets. After calcination, a high-quality structure with stable structure and high degree of crosslinking was formed (Figure 1).

To confirm the crystal structure of samples, the XRD patterns (Figure 2) of ZCM and ZCMG were recorded with the diffraction angle (2θ) range from 10° to 80° . The diffraction peaks at 23.26° , 26.41° , 28.38° , 33.71° , 36.59° , 40.19° , 41.80° , 43.46° , 47.14° , 54.67° , 58.72° , 60.04° , 63.35° , and 64.58° are all found in the monoclinic crystalline CoMoO_4 (JCPDS No. 21-0868), corresponding to (021), (002), (-311), (022), (400), (003), (222) (-223), (421), (440), (024), (-352), (-443), and (243) crystal planes. The diffraction peaks at 28.34° (011), 353.69° (210), and 57.72° (11-4) are consistent of the crystal planes of the MoO_3 standard card (JCPDS No. 47-1320). In addition, the diffraction peaks at 49.57° and 61.87° correspond to the (110) and (111) crystal planes of the ZnO standard card (JCPDS No. 16-3382), respectively. The peak at 25° represents the existence of rGO [34], and because of the overlap between the peaks of ZCM and rGO, the position of the peak was slightly shifted, and its intensity was also weakened due to the decrease in crystallinity. The above results show that ZCMG nanostructures belong to the multi-phase nature.

Figure 3 shows the SEM images of the ZCM, and triangular sheets are adhered to each other and grown on the NF uniformly, which possess the length of about 400–500 nm and thickness of around 60 nm. Usually, rGO has morphology modulating effect [35], and with the aid of rGO matrix, the ZCM nanosheets grow uniformly in a two-dimensional direction. Therefore, in the SEM images of ZCMG (Figure 4a,b), ultra-thin nanosheets with 600–700 nm in length and a thickness of around 13 nm are densely and vertically grown on NF. These nanosheets interlaced and connected to form mesh structure without stacking and ensures the large specific surface area, which increases the electrochemically active

sites and maximizes exposure of the active surface compared to ZCM. Such a structure not only accelerates the occurrence of redox reactions and expands the contact area between electrode and electrolyte, but it also effectively promotes the transfer of charge and diffusion of electrolyte, which is conducive to electrochemical reactions [36].

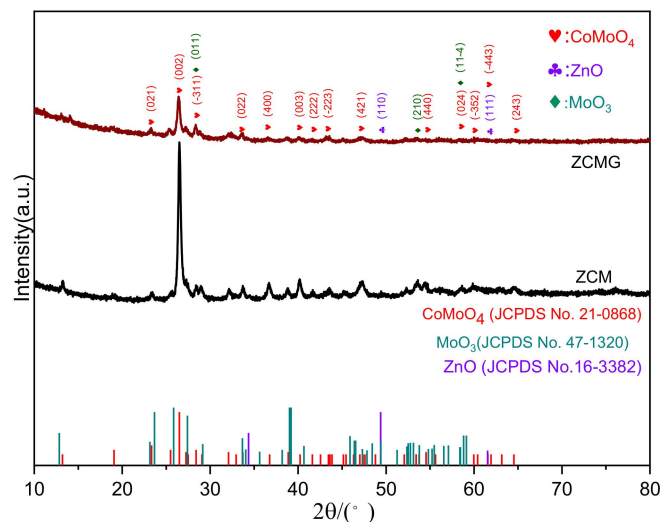


Figure 2. XRD patterns of ZCM and ZCMG.

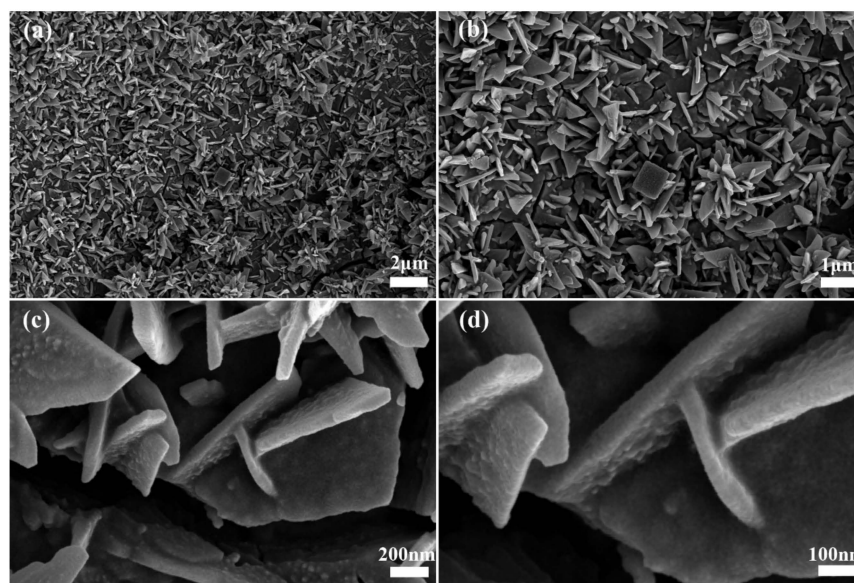


Figure 3. SEM images of ZCM. (a) 5 K magnification, (b) 10 K magnification, (c) 50 K magnification and (d) 100 K magnification.

The microstructure of ZCMG was characterized by TEM and the results are shown in Figure 5. A distinct nanosheet structure can be observed in Figure 5a, which is consistent with the SEM results, and the obvious wrinkle structure indicated the presence of rGO. Combined with the SEM results, the ZCM nanosheets with a certain thickness are deposited on NF with rGO in a co-deposition manner to form uniform nanosheets. HR-TEM images of ZCMG show lattice spacings of 0.24, 0.32 and 0.34 nm, corresponding to the (-223), (-352) and (243) planes of CoMoO_4 , respectively. A lattice spacing of 0.25 nm belongs to the (20-1) plane of MoO_3 , and lattice spacing of 0.27 nm is consistent with the (110) plane of ZnO . In addition, the EDS pattern of ZCMG (Figure 5d) demonstrates the presence of Zn, Co, Mo, and C, and these elements are uniformly distributed throughout the nanosheets, in agreement with the SEM and TEM images. All the results prove the successful preparation

of ZCMG. Selected area electron diffraction (SAED) pattern of ZCMG in Figure 5e can be indexed to the (022) and (024) planes of CoMoO_4 [37], and the SAED pattern of ZCM in Figure S1 with a diffraction ring are ascribed to the (222) and (243) planes for CoMoO_4 , consistent with the XRD results.

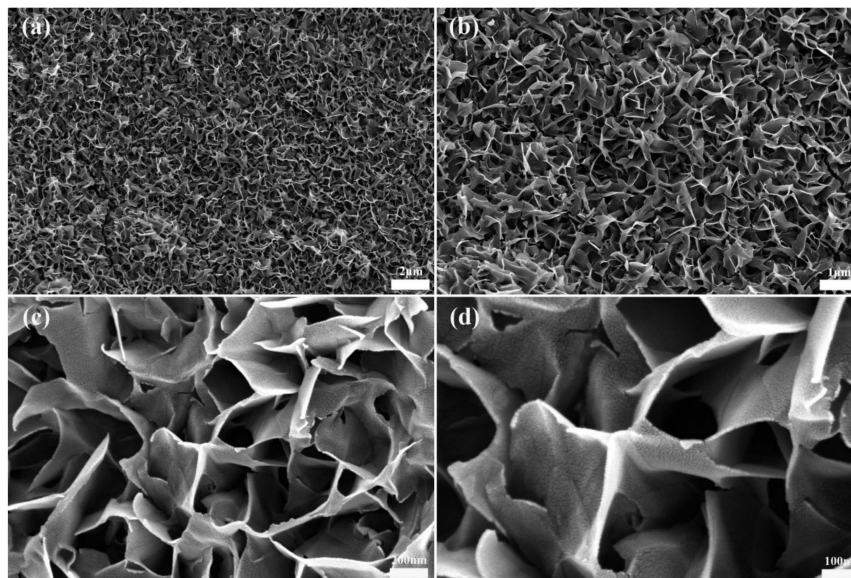


Figure 4. SEM images of ZCMG. (a) 5 K magnification, (b) 10 K magnification, (c) 50 K magnification and (d) 100 K magnification.

BET analysis of nitrogen adsorption–desorption isotherm was carried out (Figure 5f) to characterize the effective surface area [38], and the BET specific surface area for ZCM and ZCMG are 115 and $162 \text{ m}^2 \text{ g}^{-1}$, respectively. Obviously, the addition of rGO leads to an enlarged effective surface area.

The chemical composition and surface states of ZCM and ZCMG were further determined by XPS analysis (Figures 6 and S2). The XPS survey shown in Figure 6a demonstrates the existence of Zn, Co, Mo, O, and C, which is consistent with the EDS results. All the peaks of Zn 2p, Co 2p, and Mo 3d have slightly shifts (about 0.45 – 0.7 eV, Figure 6b–d) due to the addition of rGO, which indicates the interaction between rGO and metal elements. In detail, Figure 6b shows the Zn 2p spectrum, as well as the two fixed peaks at 1022.6 and 1045.7 eV, which are accredited to Zn $2p_{3/2}$ and Zn $2p_{1/2}$, respectively, for Zn^{2+} oxidation states in ZCMG [6]. As for the Co 2p spectrum (Figure 6c), the peaks at 781.59 and 797.27 eV originate from Co $2p_{1/2}$ and Co $2p_{3/2}$, indicating the presence of Co^{2+} and Co^{3+} , in addition to the two satellite peaks at 788.29 and 804.13 eV (identified as “Sat.”) [17]. The C 1s spectrum of ZCMG (Figure S2a) shows three distinct peaks at 284.79 , 286.13 and 287.27 eV, corresponding to the oxygenated carbon species: C–C, C–O [39], and C=O [18], separately. The Mo 3d spectrum (Figure 6d) corresponds to the two main peaks at 232.80 and 235.95 eV with a width of 3.2 eV, which are ascribed to Mo $3d_{5/2}$ and Mo $3d_{3/2}$, implying the present of Mo^{6+} [19]. The O 1s spectrum of ZCMG (Figure S2b) is fixed with three components, and the peaks at 530.93 , 531.50 and 533.48 eV are related to the metal–oxygen bonds (O1), as well as adsorbed water on or within the surface (O2) and OH^- (O3), respectively. The XPS results indicate the presence of different cations with multiple valence (Zn^{2+} , Mo^{6+} , Co^{2+} and Co^{3+}), and it facilitates the occurrence of redox process.

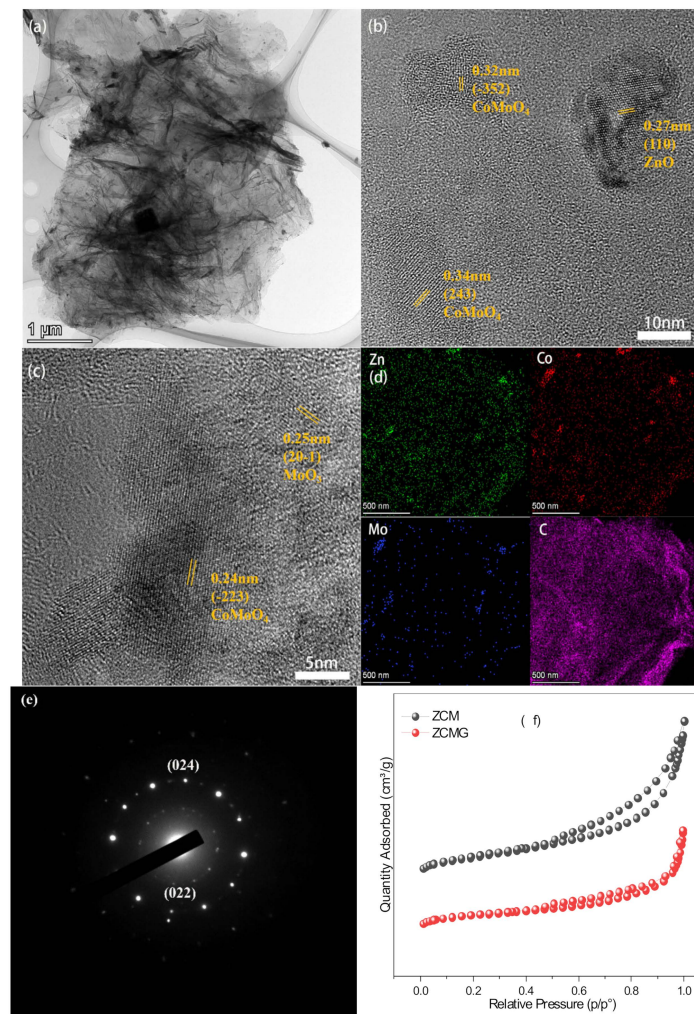


Figure 5. (a–c) TEM images of ZCMG. (d) EDS mapping of ZCMG for elements Zn, Co, Mo and C. (e) SAED pattern of ZCMG. (f) BET analysis of nitrogen adsorption-desorption isotherm curves.

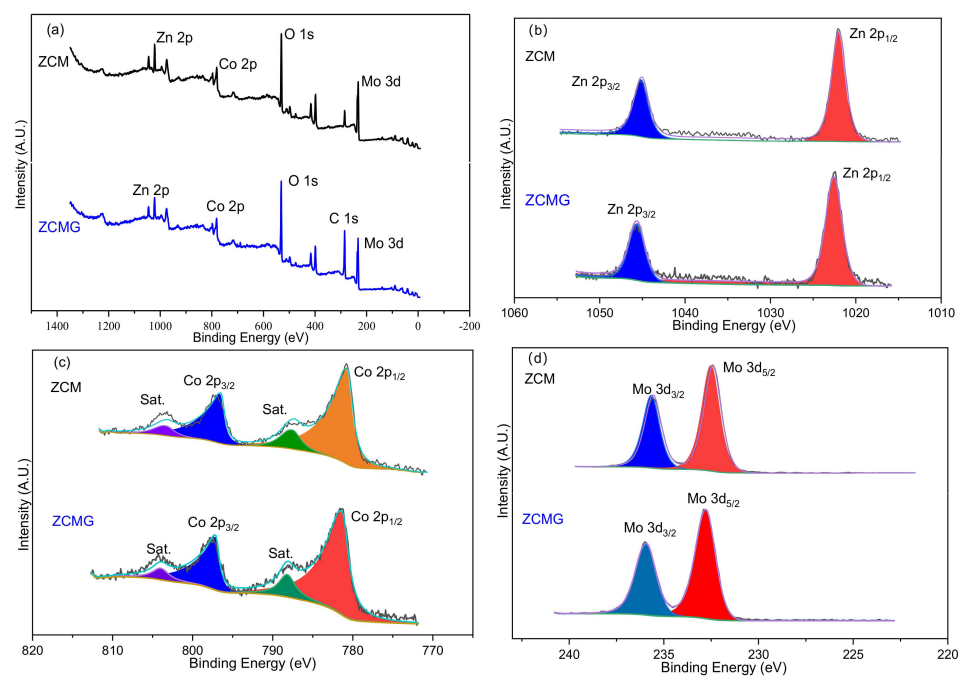


Figure 6. XPS spectra of ZCM and ZCMG. (a) XPS Survey, (b) Zn 2p, (c) Co 2p, (d) Mo 3d.

The electrochemical properties of ZCM and ZCMG were evaluated in a three-electrode measurement with 2 M KOH aqueous. Figure 7a shows the CV profiles of ZCM and ZCMG in voltage range of 0–0.65 V at a scan rate of 10 mV s^{-1} . By contrast, the ZCMG displays larger CV curve closure area and higher peak current, indicating the larger specific capacity of ZCMG. Figure 7b,d depict the CV curves of ZCM and ZCMG at different scan rates, and distinct redox peaks indicate their typical Faradaic characteristics [21,40]. As a result of the electrode polarization [41], the reduction and oxidation peaks of the redox couples shifted toward low and high potential direction, respectively, as the scanning rates increased from 5 to 50 mV s^{-1} . In addition, the shape of CV curve does not change as the scan rate increases, meaning the good rate capability and rapidly reversible Faradaic reactions. Figure 7c,e show the constant current charge/discharge curves of ZCM and ZCMG at different current densities, respectively. The charge/discharge plateau in the GCD curves corresponds to the redox peak in CV curves, and the highly symmetrical GCD curve indicates the high reversible Faradaic redox reaction. The specific capacity of ZCM and ZCMG at different current densities are shown in Figure 7f. By contrast, ZCMG exhibits higher specific capacity due to the ultra-thin nanosheet structure, which is beneficial to the redox reaction, indicating sufficient charge storage capacity. As the current density increases from 1 to 10 A g^{-1} , the specific capacity of ZCMG decreases from 713 to 572 C g^{-1} with a rate performance of 80.2%, which is still much higher than that of ZCM (69.1%). The excellent electrochemical performance of ZCMG may benefit from the ultra-thin and interconnected nanosheets, which ensure larger specific surface area and more active sites than ZCM nanosheets, shorten electron transport path during charge/discharge process, and accelerate the electron diffusion between electrolyte and active materials.

The electrochemical impedance spectroscopy (EIS) of ZCM and ZCMG are further investigated at an amplitude of 5 mV and depicted as Nyquist plots. The Nyquist plots (inset of Figure 7a) could be divided into two regions: straight line in low-frequency and semicircle in high-frequency [42]. The slope of the straight line of ZCMG (74°) is larger than that of ZCM (70°), meaning the smaller ionic diffusion resistance (R_W) of ZCMG, indicating the faster electron transport and ion diffusion during charge/discharge process. In addition, smaller semicircular diameter of ZCMG electrode could be observed, and it means the smaller charge transfer resistance (R_{ct}) between the ZCMG electrode and electrolyte. Besides, the intercept value on the X-axis represents the intrinsic resistance (R_s) [43] of electrode and electrolyte. The R_s of ZCMG (0.96Ω) is smaller than that of ZCM (1.56Ω), implying that ZCMG has stronger ion diffusion and charge transfer ability during the redox reaction. The electrochemical properties of ZCMG are also superior compared to those of related electrode materials reported in recent years (Table 1). By comparison, we combined the advantages of ternary metal oxides and rGO. For example, compared with single metal oxides and binary metal oxides, more elements participated in the redox reaction, and hence displayed higher electrochemical activity. The addition of rGO improved the conductivity and cycle performance of as-prepared materials.

To investigate the feasibility of ZCMG as electrode material, asymmetric supercapacitors (ASCs) were assembled using the ZCMG cathode and an activated carbon (AC) anode. A value of 2M KOH aqueous solution was used as electrolyte, and cellulose filter paper acted as separator. The CV curves of ZCMG and AC at 20 mV s^{-1} are shown in Figure 8a, where the voltage range of AC electrode is -1.0 – 0 V , and the voltage range of ZCMG is 0 – 0.65 V . Therefore, the voltage limit value of ASC is 1.65 V . The CV curves and GCD curves of the AC electrode are shown in Figure S3a,b, and the quasi-rectangular shape CV profile of AC indicates the typical double-layer capacity. The CV curves of ASC (Figure 8b) were tested in a voltage window from 1.0 to 1.6 V with a scan rate of 10 mV s^{-1} , and a trailing was observed when the voltage exceeded 1.5 V , probably due to the electrolyte decomposition [41]. Therefore, the operating voltage range of 0 – 1.5 V is selected. Figure 8c shows the CV curves of the ASC at different scan rates, and the CV curves shape do not change as the scan rate variation, indicating its good rate performance. Figure 8d shows the GCD curves of ASCs at different current densities, and the almost symmetric curves indicates

that ASC have good Coulombic efficiency. The specific capacity values of the device are calculated from the GCD curves and shown in Figure 8e, which displays a decrease trend (68, 51, 38, 31, 26 and 25 C g⁻¹) with the increase in current densities due to the high ion diffusion resistance and slow electrolyte penetration at higher current densities [8]. In addition, the CV and GCD curves of ZCM//AC ASC are depicted in Figure S3c,d, and they showed poor performance than these of ZCMG//AC ASC.

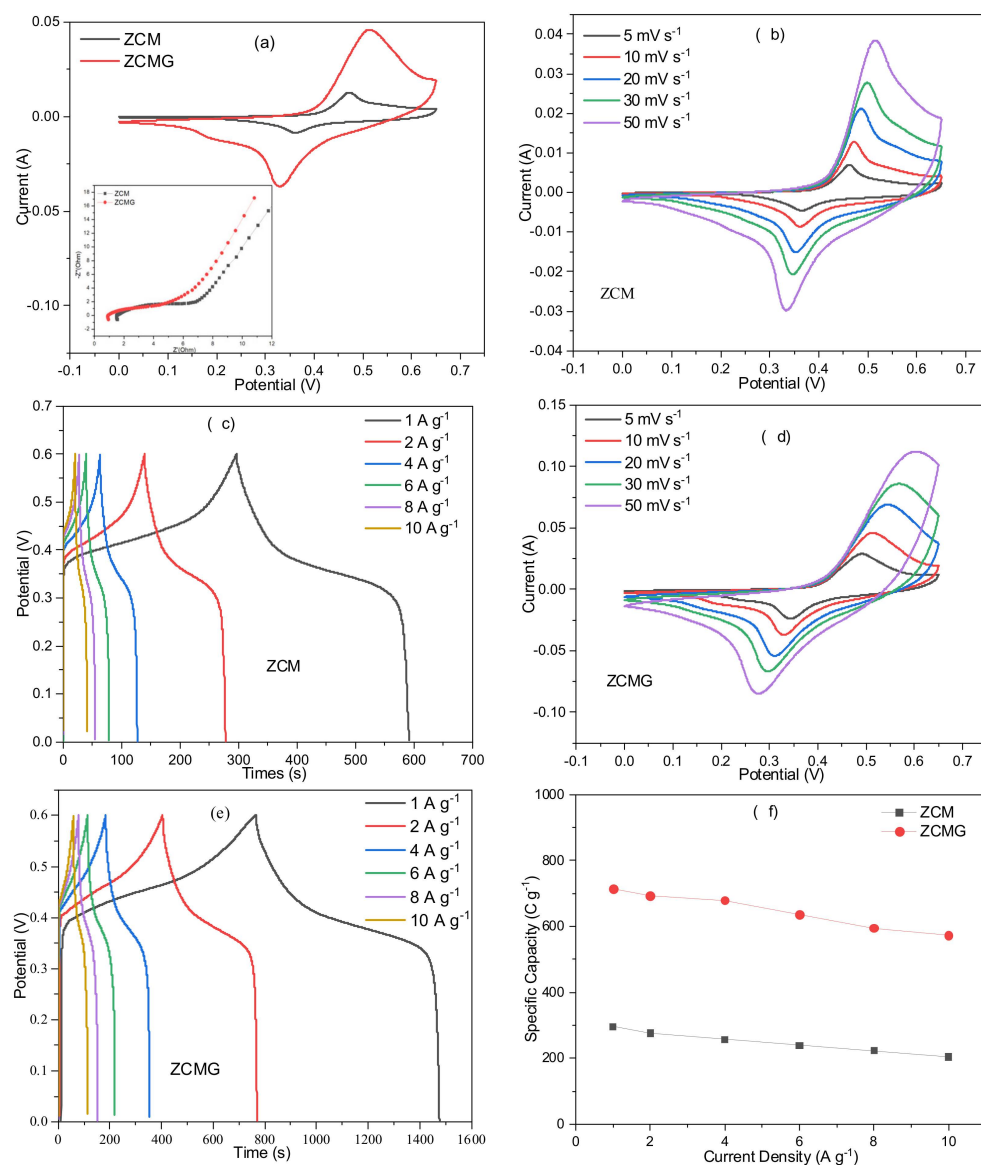


Figure 7. (a) CV plots of ZCM and ZCMG at 10 mV s⁻¹ (Inset shows the Nyquist plots of ZCM and ZCMG from 0.01 Hz to 100 kHz). (b) CV plots of ZCM at different scan rates. (c) GCD plots of ZCM at different current densities. (d) CV plots of ZCMG at different scan rates. (e) GCD plots of ZCMG at different current densities. (f) Specific capacity plots of ZCM and ZCMG at different current densities.

Cycling stability is a key factor in evaluating ASC devices, herein, 1000 cycles are performed at a current density of 1 A g⁻¹ (Figure 8f), and the capacity retention rate of ZCMG//AC ASC was 95%, indicating that the ASC has good cycling stability. Figure 8g shows the Ragone plot of energy density and power density of ASCs. The optimal energy density of 14 Wh kg⁻¹ is achieved when the power density is 750 W kg⁻¹, and even 5.23 Wh kg⁻¹ when the power density is 7500 W kg⁻¹. Furthermore, two ASCs were assembled and connected in series. After charging, the device can power a 5 mm red

circular light-emitting diode (LED lamp, 2 V, 20 mA), and the LED lamp can be lit up for at least 120 s, indicating the potential applications of the ASC devices.

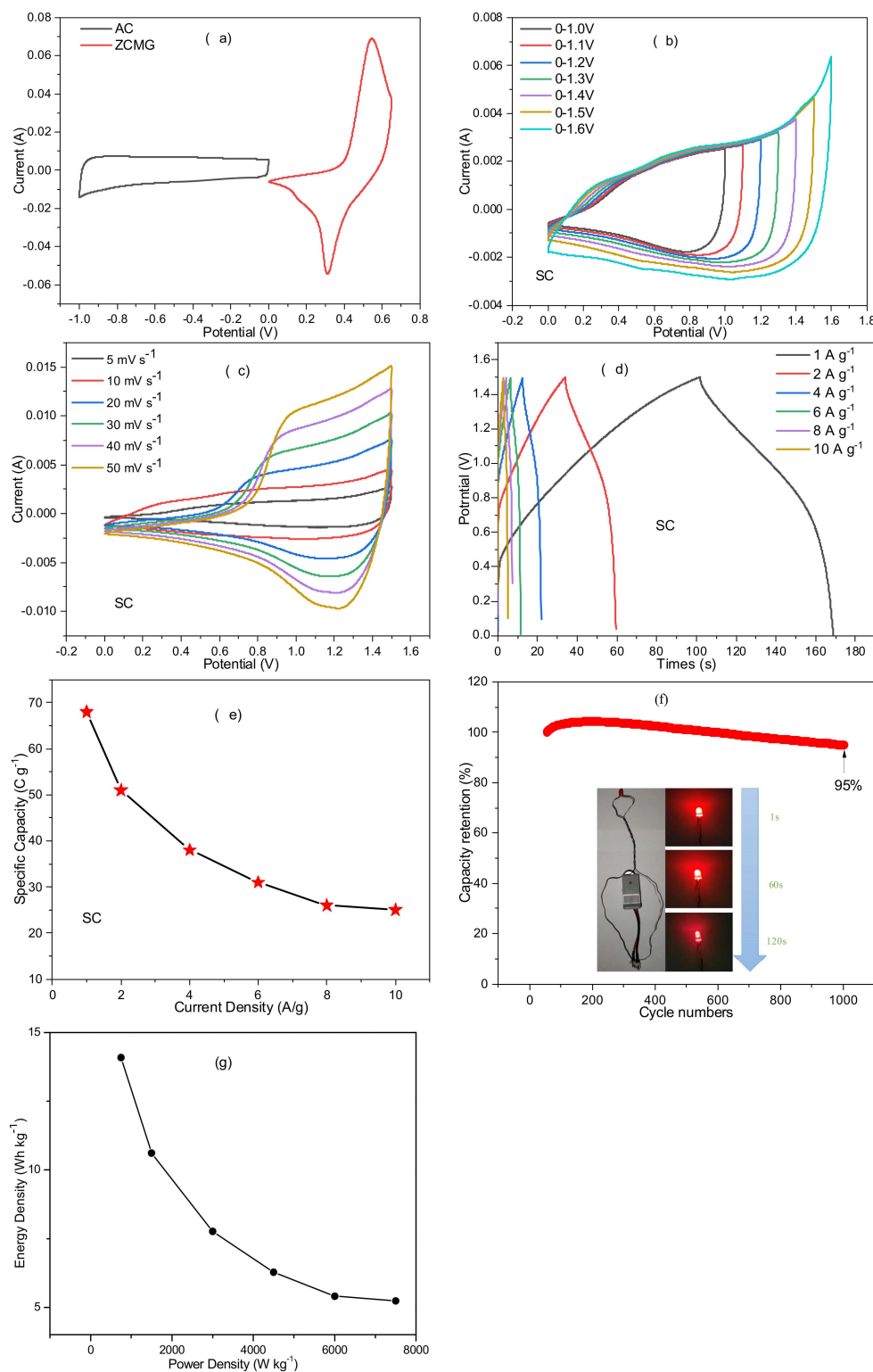


Figure 8. (a) CV plots of ZCMG and AC electrodes at 20 mV s⁻¹. (b) CV plots of ASCs at different voltage ranges. (c) CV plots of ASCs at different scan rates. (d) GCD plots of ASCs at different current densities. (e) Specific capacity plots of ASCs at different current densities. (f) Cycling performance of ASCs at 1 A g⁻¹, the inset shows the physical demonstration of driving LED lamp with two hybrid SCs. (g) Ragone diagram of ASCs.

Table 1. Comparison of relevant electrode materials reported in recent years.

Electrode Materials	Specific Capacitance (F g ⁻¹) /Specific Capacity (C g ⁻¹)	Current Density	Ref.
CuZnCo	430 F g ⁻¹	1 A g ⁻¹	[44]
CoNiMn	612 F g ⁻¹	0.5 A g ⁻¹	[20]
Ni _{0.5} Mn _{0.5} Co ₂ O ₄ @Co ₃ O ₄	931 F g ⁻¹	1 A g ⁻¹	[45]
Co ₃ O ₄ /rGO	1152 F g ⁻¹	1 A g ⁻¹	[46]
CoAl-LDH/graphene	864 F g ⁻¹	1 A g ⁻¹	[47]
ZnFe ₂ O ₄ /rGO	352.9 F g ⁻¹	1 A g ⁻¹	[48]
NiFe ₂ O ₄ /rGO	584.63 F g ⁻¹	1 A g ⁻¹	[49]
MnCo ₂ O ₄ @NiO	508.3 F g ⁻¹	1 A g ⁻¹	[50]
Zn-Co-Mo	384 F g ⁻¹	60 mA cm ⁻²	[23]
ZCMG	713 C g ⁻¹	1 A g ⁻¹	This work

4. Conclusions

In summary, we designed a ZCMG ultra-thin nanosheet arrays-based cathode material for asymmetric supercapacitor by one-step hydrothermal method. The introduction of rGO adjusted the morphology of nanosheets, enlarged the specific area, and improved the conductivity, which were conducive to the redox reaction. In consequence, ZCMG electrode material presented better specific capacity (1189 F g⁻¹, 713 C g⁻¹) than that of ZCM (492 F g⁻¹, 295 C g⁻¹) at 1 A g⁻¹. Furthermore, the rate performance of ZCMG electrode material (80.2%) was also better than that of ZCM (69.1%) at high current density, and the maximum specific capacity was 68 C g⁻¹ (1 A g⁻¹) when assembled into ZCMG//AC ASC. Simultaneously, it displayed the capacity retention rate of 95% after 1000 cycles, indicating good cycling stability. The prepared ZCMG//AC device exhibited an energy density of 14 Wh kg⁻¹ at a power density of 750 W kg⁻¹ and maintains 5.23 Wh kg⁻¹ at 7500 W kg⁻¹. All the results demonstrated that ZCMG could be used in SCs, and modification of ZCMG are currently under investigation to further improve their performance.

Supplementary Materials: The following supporting information can be downloaded at: <https://www.mdpi.com/article/10.3390/batteries9030158/s1>. Figure S1. SAED pattern of ZCM. Figure S2. XPS spectra of ZCMG. (a) C 1 s and (b) O 1 s. Figure S3. (a) CV plots of AC at different scan rates. (b) GCD plots of AC at different current densities. (c) CV plots of ZCM//AC ASC at different scan rates. (d) GCD plots of ZCM//AC ASC at different current densities.

Author Contributions: Conceptualization, J.W. and S.L.; Methodology, S.L. and S.H.; Validation, Y.X.; Formal Analysis, Y.X.; Investigation, S.L.; Resources, J.W.; Data Curation, J.W.; Writing—Original Draft Preparation, S.L.; Writing—Review and Editing, J.W.; Visualization, Y.X.; Supervision, L.X.; Project Administration, X.P.; Funding Acquisition, J.W. All authors have read and agreed to the published version of the manuscript.

Funding: The Natural Science Foundation of Hunan Province, China (Nos. 2020JJ4505, 2017JJ3256), National Natural Science Foundation of China (Nos. 21764006, 51862008, 52064014), and the Research Foundation of Jishou University of Hunan Province, China (No. Jdy21039).

Data Availability Statement: The data are available upon request from the corresponding author.

Conflicts of Interest: The authors declare no conflict of interest.

References

1. Li, M.; Luo, Y.; Jia, C.; Zhang, Q.; Luo, G.; Zhao, L.; Boukherroub, R.; Jiang, Z. Facile synthesis of bimetal nickel cobalt phosphate nanostructures for high-performance hybrid supercapacitors. *J. Alloys Compd.* **2022**, *893*, 162340. [[CrossRef](#)]
2. Rehman, J.; Eid, K.; Ali, R.; Fan, X.; Murtaza, G.; Faizan, M.; Laref, A.; Zheng, W.; Varma, R.S. Engineering of transition metal sulfide nanostructures as efficient electrodes for high-performance supercapacitors. *ACS Appl. Nano Mater.* **2022**, *5*, 6481–6498. [[CrossRef](#)]
3. Wang, C.; Zhang, D.; Liu, S.; Yamauchi, Y.; Zhang, F.; Kaneti, Y.V. Ultrathin nanosheet-assembled nickel-based metal–organic framework microflowers for supercapacitor applications. *Chem. Commun.* **2022**, *58*, 1009–1012. [[CrossRef](#)] [[PubMed](#)]
4. Wu, C.; Chen, L.; Lou, X.; Ding, M.; Jia, C. Fabrication of cobalt-nickel-zinc ternary oxide nanosheet and applications for supercapacitor electrode. *Front. Chem.* **2018**, *6*, 597. [[CrossRef](#)] [[PubMed](#)]
5. Zhang, X.; Wang, J.; Ji, X.; Sui, Y.; Wei, F.; Qi, J.; Meng, Q.; Ren, Y.; He, Y. Nickel/cobalt bimetallic metal-organic frameworks ultrathin nanosheets with enhanced performance for supercapacitors. *J. Alloys Compd.* **2020**, *825*, 154069. [[CrossRef](#)]
6. Dai, M.; Zhao, D.; Wu, X. Research progress on transition metal oxide based electrode materials for asymmetric hybrid capacitors. *Chin. Chem. Lett.* **2020**, *31*, 2177–2188. [[CrossRef](#)]
7. Han, D.; Xu, P.; Jing, X.; Wang, J.; Song, D.; Liu, J.; Zhang, M. Facile approach to prepare hollow core–shell NiO microspheres for supercapacitor electrodes. *J. Solid State Chem.* **2013**, *203*, 60–67. [[CrossRef](#)]
8. Naeem, F.; Naeem, S.; Zhao, Z.; Shu, G.; Zhang, J.; Mei, Y.; Huang, G. Atomic layer deposition synthesized ZnO nanomembranes: A facile route towards stable supercapacitor electrode for high capacitance. *J. Power Source* **2020**, *451*, 227740. [[CrossRef](#)]
9. Zhang, H.; Geng, S.; Ouyang, M.; Mao, M.; Xie, F.; Riley, D.J. Using metal cation to control the microstructure of cobalt oxide in energy conversion and storage applications. *Small* **2022**, *18*, e2106391. [[CrossRef](#)]
10. Wu, F.; Cui, F.; Ma, Q.; Zhang, J.; Qi, X.; Cui, T. Facile construction of hexagonal Co₃O₄ as the electrode for high-performance supercapacitor. *Mater. Lett.* **2022**, *324*, 132791. [[CrossRef](#)]
11. Wang, Y.; Pan, A.; Zhu, Q.; Nie, Z.; Zhang, Y.; Tang, Y.; Liang, S.; Cao, G. Facile synthesis of nanorod-assembled multi-shelled Co₃O₄ hollow microspheres for high-performance supercapacitors. *J. Power Source* **2014**, *272*, 107–112. [[CrossRef](#)]
12. Rizwan, A.; Ghulam, N.; Faisal, A.; Faiza, N.; Muhammad, I.K.; Tahir, I.; Muhammad, T.; Wajid, A.; Naeem, S.A.; Anum, N.; et al. Controlled growth of Mo-Doped NiO nanowires with enhanced electrochemical performance for supercapacitor applications. *Mater. Sci. Eng. B* **2022**, *284*, 115881.
13. Xiong, S.; Weng, S.; Tang, Y.; Qian, L.; Xu, Y.; Li, X.; Lin, H.; Xu, Y.; Jiao, Y.; Chen, J. Mo-doped Co₃O₄ ultrathin nanosheet arrays anchored on nickel foam as a bi-functional electrode for supercapacitor and overall water splitting. *J. Colloid Interface Sci.* **2021**, *602*, 355–366. [[CrossRef](#)] [[PubMed](#)]
14. Sun, H.; Zhu, J.; Daniel, B.; Peng, L.; Xu, Y.; Imran, S.; Huang, Y.; Duan, X. Hierarchical 3D electrodes for electrochemical energy storage. *Nat. Rev. Mater.* **2018**, *4*, 45–60. [[CrossRef](#)]
15. Shi, Q.; Zhang, Q.; Yang, Y.; Zang, Q.; Xiao, Z.; Zong, L.; Wang, K. In Situ construction of a heterostructured Zn–Mo–Ni–O–S hollow microflower for high-performance hybrid supercapacitors. *ACS Appl. Nano Mater.* **2021**, *4*, 801–809. [[CrossRef](#)]
16. Sumanta, S.; Thi, T.N.; Shim, J.-J. Mesoporous Fe–Ni–Co ternary oxide nanoflake arrays on Ni foam for high-performance supercapacitor applications. *J. Ind. Eng. Chem.* **2018**, *63*, 181–190.
17. Zhu, Y.; Ji, X.; Yin, R.; Hu, Z.; Qiu, X.; Wu, Z.; Liu, Y. Nanorod-assembled NiCo₂O₄ hollow microspheres assisted by an ionic liquid as advanced electrode materials for supercapacitors. *RSC Adv.* **2017**, *7*, 11123–11128. [[CrossRef](#)]
18. Maitra, A.; Das, A.K.; Bera, R.; Karan, S.K.; Paria, S.; Si, S.K.; Khatua, B.B. An approach to fabricate PDMS encapsulated all-solid-state advanced asymmetric supercapacitor device with vertically aligned hierarchical Zn–Fe–Co ternary oxide nanowire and nitrogen doped graphene nanosheet for high power device applications. *ACS Appl. Mater. Interfaces* **2017**, *9*, 5947–5958. [[CrossRef](#)]
19. Acharya, J.; Ko, T.H.; Seong, J.; Seo, M.; Khil, M.; Kim, H.; Kim, B.-S. Hybrid electrodes based on Zn–Ni–Co ternary oxide nanowires and nanosheets for ultra-high-rate asymmetric supercapacitors. *ACS Appl. Nano Mater.* **2020**, *3*, 8679–8690. [[CrossRef](#)]
20. Yuan, C.; Zhang, L.; Hou, L.; Pang, G.; Zhang, X. Green template-free synthesis of mesoporous ternary CoNi–Mn oxide nanowires towards high-performance electrochemical capacitors. *Part. Part. Syst. Char.* **2014**, *31*, 778–787. [[CrossRef](#)]
21. Hussain, I.; Mohamed, S.G.; Ali, A.; Abbas, N.; Ammar, S.M. Uniform growth of Zn–Mn–Co ternary oxide nanoneedles for high-performance energy-storage applications. *J. Electroanal. Chem.* **2019**, *837*, 39–47. [[CrossRef](#)]
22. Zhang, J.; Li, C.; Fan, M.; Ma, T.; Chen, H.; Wang, H. Two-dimensional nanosheets constituted trimetal Ni–Co–Mn sulfide nanoflower-like structure for high-performance hybrid supercapacitors. *Appl. Surf. Sci.* **2021**, *565*, 150482. [[CrossRef](#)]
23. Su, W.; Miao, R.; Tao, B.; Miao, F. High-performance symmetric supercapacitor based on flower-like zinc-cobalt-molybdenum hybrid metal oxide. *Ionics* **2019**, *25*, 5419–5427. [[CrossRef](#)]
24. Shmatko, V.; Leontyeva, D.; Nevzorova, N.; Smirnova, N.; Brzhezinskaya, M.; Yalovega, G. Interaction between NiO_x and MWCNT in NiO_x/MWCNTs composite: XANES and XPS study. *J. Electron. Spectrosc.* **2017**, *220*, 76–80. [[CrossRef](#)]
25. Liu, Z.; Hu, J.; Shen, F.; Tian, D.; Huang, M.; He, J.; Zou, J.; Zhao, L.; Zeng, Y. Trichoderma bridges waste biomass and ultra-high specific surface area carbon to achieve a high-performance supercapacitor. *J. Power Source* **2021**, *497*, 229880. [[CrossRef](#)]
26. Mohammad, B.; Parisa, S.; Majid, S.; Mohammad, H.; Di Bartolomeo, A. ZnFe₂O₄ nanorods on reduced graphene oxide as advanced supercapacitor electrodes. *J. Alloys Compd.* **2021**, *860*, 158497.

27. Zhang, X.; Zhang, J.; Kong, S.; Zhu, K.; Yan, J.; Ye, K.; Wang, G.; Cheng, K.; Zhou, L.; Cao, D. A novel calendula-like MnNb₂O₆ anchored on graphene sheet as high-performance intercalation pseudocapacitive anode for lithium-ion capacitors. *J. Mater. Chem. A* **2019**, *7*, 2855–2863. [[CrossRef](#)]
28. Yuan, J.; Yao, D.; Jiang, L.; Tao, Y.; Che, J.; He, G.; Chen, H. Mn-doped NiMoO₄ mesoporous nanorods/reduced graphene oxide composite for high-performance all-solid-state supercapacitor. *ACS Appl. Energy Mater.* **2020**, *3*, 1794–1803. [[CrossRef](#)]
29. Kulurumotlakatla, D.K.; Yedluri, A.K.; Kim, H.-J. Hierarchical NiCo₂S₄ nanostructure as highly efficient electrode material for high-performance supercapacitor applications. *J. Energy Storage* **2020**, *31*, 101069. [[CrossRef](#)]
30. Yedluri, A.K.; Kim, H.-J. Wearable super-high specific performance supercapacitors using a honeycomb with folded silk-like composite of NiCo₂O₄ nanoplates decorated with NiMoO₄ honeycombs on nickel foam. *Dalton Trans.* **2018**, *47*, 15545–15554. [[CrossRef](#)]
31. Anil, K.Y.; Dasha, K.K.; Kim, H.-J. Facile preparation of a highly efficient NiZn₂O₄–NiO nanoflower composite grown on Ni foam as an advanced battery-type electrode material for high-performance electrochemical supercapacitors. *Dalton Trans.* **2020**, *49*, 3622–3629. [[CrossRef](#)] [[PubMed](#)]
32. Acharya, J.; Ojha, G.P.; Kim, B.S.; Pant, B.; Park, M. Modish designation of hollow-tubular rGO–NiMoO₄@Ni–Co–S hybrid core-shell electrodes with multichannel superconductive pathways for high-performance asymmetric supercapacitors. *ACS Appl. Mater. Interfaces* **2021**, *13*, 17487–17500. [[CrossRef](#)] [[PubMed](#)]
33. Mei, J.; Liao, T.; Sun, Z. Two-dimensional metal oxide nanosheets for rechargeable batteries. *J. Energy Chem.* **2018**, *27*, 117–127. [[CrossRef](#)]
34. Velmurugan, V.; Srinivasarao, U.; Ramachandran, R.; Saranya, M.; Nirmala Grace, A. Synthesis of tin oxide/graphene (SnO₂/G) nanocomposite and its electrochemical properties for supercapacitor applications. *Mater. Res. Bull.* **2016**, *84*, 145–151. [[CrossRef](#)]
35. Aadithya, J.; Tamil, S.; Craig, J.N.; Sudipta, S. Scalable ternary hierarchical microspheres composed of PANI/rGO/CeO₂ for high performance supercapacitor applications. *Carbon* **2019**, *151*, 192–202.
36. Poochai, C.; Sriprachuabwong, C.; Odtipinta, J.; Lohitkarn, J.; Pasakon, P.; Primpray, V.; Maeboonruan, N.; Lomas, T.; Wisitsoraat, A.; Tuantranont, A. Alpha-MnO₂ nanofibers/nitrogen and sulfur-co-doped reduced graphene oxide for 4.5 V quasi-solid state supercapacitors using ionic liquid-based polymer electrolyte. *J. Colloid Interface Sci.* **2021**, *583*, 734–745. [[CrossRef](#)]
37. Kumar, Y.A.; Al, A.; Pallavolu, M.R.; Rao, S.S.; Nallapureddy, R.R.; Ramakrishna, S. Multiple structural defects in poor crystalline nickel-doped tungsten disulfide nanorods remarkably enhance supercapacitive performance. *Int. J. Energ. Res.* **2022**, *46*, 14227–14239. [[CrossRef](#)]
38. Kumar, Y.A.; Kumar, K.D.; Kim, H.-J. Reagents assisted ZnCo₂O₄ nanomaterial for supercapacitor application. *Electrochim. Acta* **2020**, *330*, 135261. [[CrossRef](#)]
39. Rabchinskii, M.K.; Ryzhkov, S.A.; Besedina, N.A.; Brzhezinskaya, M.; Malkov, M.N.; Stolyarova, D.Y.; Arutyunyan, A.F.; Struchkov, N.S.; Saveliev, S.D.; Diankin, I.D. Guiding graphene derivatization for covalent immobilization of aptamers. *Carbon* **2022**, *196*, 264–279. [[CrossRef](#)]
40. Zhang, P.; He, H.; Peng, Y.; Wu, Y. Engineering RuO₂ on CuCo₂O₄/CuO nanoneedles as multifunctional electrodes for the hybrid supercapacitors and water oxidation catalysis. *J. Alloys Compd.* **2020**, *832*, 154962. [[CrossRef](#)]
41. Cao, Y.; An, L.; Liao, L.; Liu, X.; Ji, T.; Zou, R.; Yang, J.; Qin, Z.; Hu, J. Hierarchical core/shell structures of ZnO nanorod@CoMoO₄ nanoplates used as a high-performance electrode for supercapacitors. *RSC Adv.* **2016**, *6*, 3020–3024. [[CrossRef](#)]
42. Yuan, Y.; Jia, H.; Liu, Z.; Wang, L.; Sheng, J.; Fei, W. A highly conductive Ni(OH)₂ nano-sheet wrapped CuCo₂S₄ nano-tube electrode with a core-shell structure for high performance supercapacitors. *Dalton Trans.* **2021**, *50*, 8476–8486. [[CrossRef](#)] [[PubMed](#)]
43. Barqi, J.; Masoudpanah, S.M.; Hasheminasari, M.; Liu, X. Nanoribbon-like NiCo₂O₄/reduced graphene oxide nanocomposite for high-performance hybrid supercapacitor. *J. Alloys Compd.* **2023**, *930*, 167509. [[CrossRef](#)]
44. Subbukalai, V.; Lee, S.-H.; Sadayappan, N.; Ryu, K. Cu–Zn–Co oxide nanoflakes on Ni-foam as a binder free electrode for energy storage applications. *Materials Letters. Mater. Lett.* **2018**, *219*, 143–147.
45. Han, C.; Xu, X.; Mu, H.; Tian, Q.; Li, Q.; Liu, Y.; Zhang, X.; Zhao, Z.; Su, X. Construction of hierarchical sea urchin-like manganese substituted nickel cobaltite@tricobalt tetraoxide core-shell microspheres on nickel foam as binder-free electrodes for high performance supercapacitors. *J. Colloid Interface Sci.* **2021**, *596*, 89–99. [[CrossRef](#)]
46. Zhao, Y.; Liu, H.; Hu, P.; Song, J.; Xiao, L. Asymmetric hybrid capacitor based on Co₃O₄ nanowire electrode. *Ionics* **2020**, *26*, 6289–6295. [[CrossRef](#)]
47. Zhang, Y.; Du, D.; Li, X.; Sun, H.; Li, L.; Bai, P.; Xing, W.; Xue, Q.; Yan, Z. Electrostatic self-assembly of sandwich-like CoAl-LDH/polypyrrole/graphene nanocomposites with enhanced capacitive performance. *ACS Appl. Mater. Interfaces* **2017**, *9*, 31699–31709. [[CrossRef](#)]
48. Yan, S.; Han, Z.; Sun, J.; Yang, X.; Hu, X.; Li, C.; Cao, B. Controllable ZnFe₂O₄/reduced graphene oxide hybrid for high-performance supercapacitor electrode. *Electrochim. Acta* **2018**, *268*, 20–26. [[CrossRef](#)]
49. Askari, M.B.; Salarzadeh, P. Binary nickel ferrite oxide (NiFe₂O₄) nanoparticles coated on reduced graphene oxide as stable and high-performance asymmetric supercapacitor electrode material. *Int. J. Hydrogen Energy* **2020**, *45*, 27482–27491. [[CrossRef](#)]
50. Cheng, B.; Zhang, W.; Yang, M.; Zhang, Y.; Meng, F. Preparation and study of porous MnCo₂O₄@NiO nanosheets for high-performance supercapacitor. *Ceram. Int.* **2019**, *45*, 20451–20457. [[CrossRef](#)]

Disclaimer/Publisher’s Note: The statements, opinions and data contained in all publications are solely those of the individual author(s) and contributor(s) and not of MDPI and/or the editor(s). MDPI and/or the editor(s) disclaim responsibility for any injury to people or property resulting from any ideas, methods, instructions or products referred to in the content.